# Two-Phase Oblique Photogrammetric Model for Automated Change Detection in Railroad Slopes

Xingning Zhu<sup>1</sup>, Ming Huang<sup>12</sup>, Lei Wang<sup>1</sup>

<sup>1</sup> School of Geomatics and Urban Spatial Informatics, Beijing University of Civil Engineering and Architecture, China - 2108160223011@stu.bucea.edu.cn

Keywords: Change detection; Oblique photographic model; Railroad slopes; Automated inspection; Point cloud processing.

#### Abstract

Railroad slope detection is crucial for railroad inspection. However, traditional stability detection methods face challenges such as high costs, subjectivity, and reliance on prior information. To address these issues, we propose an automatic change detection algorithm based on a two-stage oblique photogrammetric model. The algorithm begins by extracting point cloud data from the structure and performs encryption and alignment preprocessing to eliminate spatial bias. It then dynamically selects core points to construct a cylindrical analysis domain, followed by comparing the differences in projected distances between the two phases of the point cloud against a preset threshold to identify changes. Experimental results demonstrate that our algorithm significantly outperforms traditional C2C and C2M methods in accurately detecting substantial changes, filtering out unrealistic alterations, adapting to various terrains, and reducing costs while enhancing efficiency. Notably, the algorithm achieves a maximum recognition accuracy of 96.825% at a threshold of 1 mm, underscoring its sophistication and effectiveness.

#### 1. Introduction

As one of the most important modes of transport in China, the state invests heavily each year to advance railroad science and technology. In 2023, national fixed asset investment in railroads exceeded 760 billion yuan, resulting in the commissioning of over 3,000 kilometers of new lines, including 2,500 kilometers of high-speed rail. This rapid expansion of the railroad network, along with the integration of old and new lines, has not only significantly reduced travel times and improved transportation efficiency but has also effectively promoted the coordinated development of regional economies and social progress (Ouyang and Yi, 2020).

Railroad slopes, as critical components of the railroad system, directly impact the safety and reliability of railroad operations (Liu et al., 2023). However, with the continuous extension of operational mileage and the accumulation of operational time, factors such as complex and variable weather conditions and geological movements can lead to permanent and irreparable damage to railroad slopes. Issues such as slope deterioration occur frequently, severely affecting the safety and stability of railroad transportation (Deng et al., 2025; Zhang et al., 2024). To ensure the stable operation of the railroad industry, it is essential to regularly monitor changes in the surrounding environment and take appropriate measures. Therefore, realizing precise location and intelligent detection of areas undergoing changes in railroad slopes is crucial.

Traditional large-scale change detection methods primarily rely on manual inspections and instrumental measurements. These include collecting 3D spatial data of the region using devices such as UAV tilt photography (Yu et al. 2022), interferometric synthetic aperture radar, and airborne or vehicle-mounted 3D laser scanners (Mukupa et al. 2017, Zhang et al. 2019). Subsequently, changes in the region are analyzed through image processing and manual interpretation. However, these methods face several challenges, including significant consumption of

human and material resources, low efficiency in data acquisition and processing, and a high degree of subjectivity (Shao et al. 2023). In recent years, target detection algorithms based on deep convolutional neural networks have gained popularity in change detection applications(Ren et al. 2016). While these techniques significantly enhance recognition accuracy and efficiency, overcoming many limitations of traditional methods, their performance can be constrained in scenarios with limited data or complex environments due to their reliance on large datasets and prior knowledge (Dong et al. 2024). In contrast to traditional methods and deep learning techniques, employing a multi-phase oblique photogrammetric model for change detection offers distinct advantages. This approach leverages precise geometric features within the model (Liu et al. 2023), minimizing the influence of subjective factors, thereby enhancing identification accuracy and stability. It allows for the accurate identification of various change areas, providing a scientific basis for timely maintenance measures.

Building on the previous discussion, we propose an automated change detection algorithm tailored for two-phase oblique photogrammetric models of slope structures. This algorithm enables automated identification and dynamic assessment of change areas by analyzing the geometric features of ioblique photogrammetric models. It begins by extracting vertex point cloud data from each structure, followed by preprocessing, and then compares and analyzes this data with multi-phase datasets to accurately identify change areas and mark their corresponding locations within the model.

In summary, our contributions are as follows:

·A key advantage of our approach is the implementation of a KD-tree data structure, which significantly enhances detection efficiency by enabling rapid spatial queries. This allows for quicker identification of relevant points within the point cloud, thereby streamlining the change detection process.

<sup>&</sup>lt;sup>2</sup> Engineering Research Center of Representative Building and Architectural Heritage Database, Beijing, China - huangming@bucea.edu.cn

· Compared to traditional manual interpretation and deep learning methods, our approach visualizes the spatial morphology and structural relationships of change areas through the oblique photogrammetric model. This not only reduces the need for manual intervention but also overcomes the limitations of data dependency, enhancing the robustness of detection in complex environments.

#### 2. Two-phase model change detection

The two-phase oblique photogrammetric model change detection algorithm proposed in this paper facilitates the detection and analysis of structural changes through a series of systematic processes. First, the vertex point cloud data from the two-phase model is up-sampled and densified to enhance point cloud density while preserving detailed features. Second, due to the differences in local coordinate systems established by the two-phase model, point cloud alignment is necessary to eliminate spatial deviations between the two sets of point cloud data, ensuring consistent spatial reference. Finally, core points are dynamically selected, and the search radius is determined based on the original point cloud data. The normal vector direction of the fitting plane is calculated using the local point cloud distribution, and a cylindrical analysis domain is constructed along this direction. The change region is identified by comparing the scalar differences of the projections specifically, the projections of each point in the two-phase point cloud within the cylindrical region against the projection of the core point along the normal vector direction. If the difference exceeds a predetermined minimum threshold, the area is classified as a change region.

#### 2.1 Preprocessing of vertex point clouds

The vertex point cloud data extracted from the oblique photogrammetric model is generated by dense matching of UAV-acquired oblique photographic images. However, this data presents two main issues: first, the distribution of vertices within the model is relatively sparse, and many triangular facets are narrow, leading to the presence of voids and gaps in the point cloud data of slope structures. Second, for comparative analysis, it is necessary to utilize data from multi-temporal models. However, differences in the local coordinate transformation matrices constructed by these various time-phase models result in deviations between the point cloud data of the two models. To address these issues, the following preprocessing steps are required.

To achieve upsampling and densification of point cloud data while preserving the original geometric features of ground objects, this study combines linear interpolation and barycentric interpolation for triangulated facet interpolation. In gently sloping areas, the longest edge P<sub>1</sub>P<sub>2</sub> of the triangular mesh is first identified, with its length denoted as L<sub>max</sub>. A preset interpolation step t is then used to dynamically calculate the segmentation number N, and interpolation points along the longest edge are generated using the linear formula:

$$Q = P_1 + \frac{i}{N} (P_2 - P_1)(i = 1, 2, ..., N),$$
 (1)

For the shortest edge  $P_1P_3$ , if the initially computed interpolation point fall outside the range of this edge, a parallel line is constructed to find intersections with neighboring edges, ensuring valid point insertions.

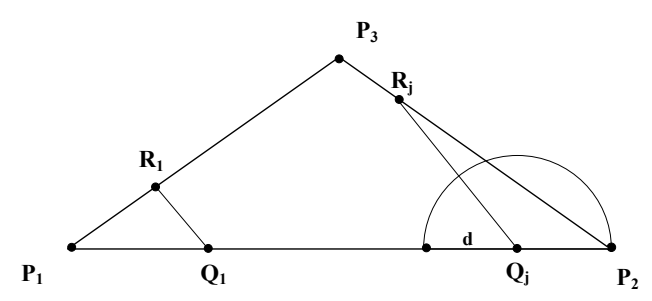


Figure 1. Schematic of linear interpolation.

In the case of concave regions, a refined interpolation method is employed based on the triangular mesh. The longest edge of the triangle, denoted as  $L_{max}$ , is used in conjunction with a preset interpolation step length. The total number of segments M is dynamically calculated, generating parameters r and s. The condition r+s<1 ensures that the interpolation points remain within the triangular region. Ultimately, the following formula is used to generate a uniform distribution of the interpolation points:

$$Q = r \cdot P_1 + s \cdot P_2 + (1 - r - s) \cdot P_3 , \qquad (2)$$

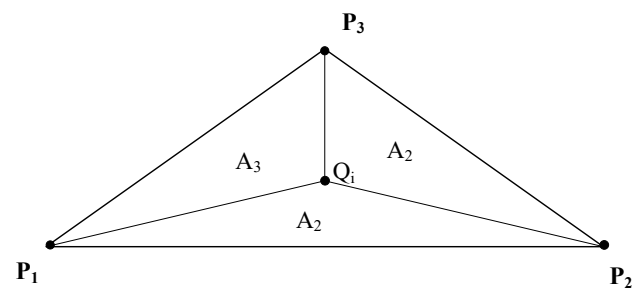


Figure 2. Schematic of center of gravity interpolation.

By adaptively employing linear interpolation in gently sloping areas and rounded corner interpolation in concave regions, this strategy facilitates accurate densification by efficiently upsampling the point cloud data while preserving the original geometric features of the ground objects.

After upsampling, the differing local coordinate systems of the two-stage model result in spatial offsets of the point cloud data within the same region, necessitating alignment and correction. Initially, the sample consensus initial alignment (SAC-IA) algorithm is employed for coarse alignment. This algorithm selects sampling points from the point cloud data by predefining the number of iterative sampling points and establishing a minimum distance threshold between them to ensure representativeness. It then identifies candidate points with similar fast point feature histograms (FPFH) eigenvalues and calculates the error Li, using a penalty function to prepare for subsequent accurate alignment, as expressed in the following formula:

$$H(l_{i}) = \begin{cases} \frac{1}{2} \| l_{i} \|^{2}, & \mu \pm \| l_{i} \| \leq m_{l} \\ \frac{1}{2} m_{l} (2 \| l_{i} \| - m_{l}), & \mu \pm \| l_{i} \| > m_{l} \end{cases}$$
(3)

where  $||l_i|| = \text{Norm of the error vector}$  $m_l = \text{Preset threshold.}$ 

Building on the coarse alignment, the generalized iterative closest point (GICP) algorithm is employed for precise alignment by integrating the local covariance matrix of the two-phase point cloud. This algorithm introduces a probabilistic model during the minimization step of the standard iterative closest point (ICP) algorithm while continuing to utilize the standard Euclidean distance to establish corresponding relationships. By ensuring alignment accuracy, the algorithm reduces complexity and enhances computational efficiency, further improving the geometric consistency of the two-phase point cloud data and accurately calculating the alignment error.

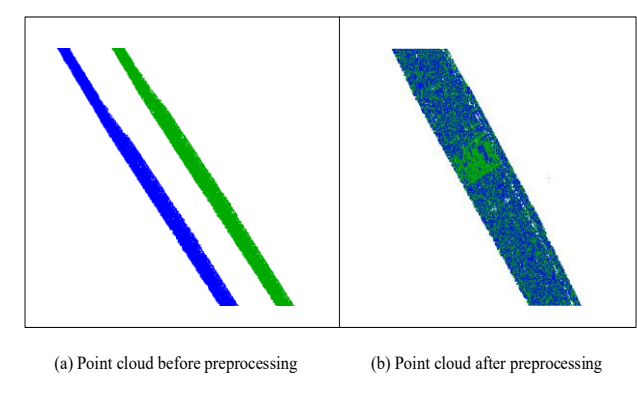


Figure 3. Two phases of point cloud data preprocessing results.

# 2.2 Selection of core points and calculation of normal vectors

Due to the high density of the upsampled and densified point cloud data, along with the geometric representativeness of the model vertex data itself, the algorithm directly uses the vertex data of the original model as the core point sampling set Qcore. The upsampled two-phase point cloud data is designated as the source point set Qori and the difference set Qdiff respectively, to ensure computational efficiency. After establishing the initial search radius r, iterative step h<sub>r</sub>, and the maximum search radius  $r_{\text{max}}$ , a radius search is conducted for each core point in the source point set Qori to obtain the local point cloud set Plocal. Next, an augmented matrix A is constructed for singular value decomposition (SVD) to derive the fitting plane parameters. Through singular value decomposition, matrix A is decomposed into the product of three matrices U,  $\Sigma$ , and V, where matrix U represents the left singular vector, matrix V is the right singular vector; and  $\Sigma$  is is the singular value matrix arranged in descending order. The plane normal vector n is determined by the third column of Vand is perpendicular to the fitting plane. The direction of the normal vector is consistently corrected according to the spatial distribution characteristics of the differential point cloud to ensure that it points in the direction of the differential point cloud. The plane fit quality parameter  $\sigma_{conf}$ is calculated using the following equation:

$$\sigma_{\text{conf}} = 2 \times \sigma_1 + 4 \times \sigma_2 , \qquad (4)$$

where  $\sigma_1, \sigma_2 = Distribution$  intensity of principal components within the plane

coefficient term = Empirical value

Each core point undergoes an iterative process to determine the optimal radius  $r_{\rm opt}$ . Ultimately, the optimal normal vector  $n_{\rm opt}$  corresponding to  $r_{\rm opt}$  is used to construct the cylindrical analysis domain.

$$r_{\text{opt}} = arg \max_{r \in \{r, r + \Delta r, \dots, r_{\text{max}}\}} \omega_{\text{conf}}^{(r)}, \qquad (5)$$

# 2.3 Establishing a cylindrical analysis domain and computing change distances

After setting the cylindrical radius  $r_{cyl}$ , both the initial cylindrical depth  $d_{start}$  and the iteration step  $h_{cyl}$  are defined as half of the cylinder radius. For points located within the cylinder  $P_{cyl}$ , two constraints must be simultaneously satisfied: the radial constraint and the axial constraint.

$$\left| n_{\text{opt}} \times \left( P_{\text{cyl}} - P_{\text{core}} \right) \right| \le d_{\text{now}} ,$$
 (6)

$$(p_{\text{cyl}} - p_{\text{core}}) - [n_{\text{opt}} \times (p_{\text{cyl}} - p_{\text{core}})] n_{\text{opt}} \le r_{\text{cyl}}, \quad (7)$$

where  $n_{opt}$  = The optimal normal vector corresponding to  $r_{opt}$ 

After identifying the set of points  $Q_{cyl}$  that meet the constraints of the cylindrical domain, the weight of each point in the variation distance calculation is determined using the following weight function, which is based on the geometric relationship between the points and the cylindrical axes:

$$\omega_i = exp\left(-\frac{\|P_i - P_{\text{core}}\|^2}{2r_{\text{cyl}}^2}\right), \ P_i \in Q_{\text{cyl}}, \tag{8}$$

where  $r_{cyl} = Radius of a cylinder$ 

According to this weighting formula, the larger the Euclidean distance between point  $P_i$  and the current core point, the smaller  $\omega_i$  will be. This reduces the influence of points that are distant from the core point in the distance calculation. Once the weights for each point are determined, the weighted average of the projected scalars of the two-phase point cloud is calculated separately according to the following formula:

$$\mu = \frac{\sum_{i=1}^{N} \omega_i t_i}{\sum_{i=1}^{N} \omega_i}, \quad t_i = n_{\text{opt}} \times (P_i - P_{\text{core}}), \tag{9}$$

where  $t_i$ = The projection scalar of the points in the cylinder to the current core point

 $\omega_i$  = Weighting coefficient for each point calculated according to Eq.(8)

The deformation estimate  $\Delta\mu$  is derived from the following formula:

 $\Delta \mu = \left| \mu_{\text{ori}} - \mu_{\text{diff}} \right|, \tag{10}$ 

where  $\mu_{ori}$  = The weighted average of the projected scalars of the source point cloud at the current core point.

 $\mu_{\text{diff}}$  = The weighted average of the projected scalars of the differential point cloud at the current core point

#### 3. Experimental process

### 3.1 Experimental data

To verify the feasibility and accuracy of the proposed automatic change detection algorithm for slope modeling, we conducted experiments using model data from the Nanwan Railway section in Xinzhou City, Shanxi Province. The process for acquiring experimental data is as follows: First, we performed multi-angle image acquisition of the railroad section using UAV aerial photography technology to ensure complete coverage and an adequate overlap rate of the images. This approach allowed us to quickly obtain high-resolution images, providing rich detail for subsequent modeling. Next, we utilized Context Capture software to convert the image data into a high-quality 3D model, enabling the construction of a two-stage railroad slope model. Finally, we extracted the vertex cloud data of the slope structures from the model by isolating the individual slope components.

Figure 4 illustrates the overall layout of the railroad section, showcasing various components such as slopes, tracks, drains, and side slopes.





Figure 4. Experimental data.

# 3.2 Change detection in slope structures

After preprocessing the point cloud data at the top of the slope structure, we employed the two-stage model change detection algorithm for analysis. The parameters of the algorithm were set as follows: the core point set  $Q_{\rm core}$  was constructed from the initial point cloud data to serve as the reference benchmark; the two-stage point cloud data were up-sampled to create the source point set  $Q_{\rm ori}$  and the differential point set  $Q_{\rm diff}$ , which were used for comparative analysis.

In the normal vector calculation stage, the initial search radius r was set to 30 cm, with an iteration step  $h_r$  of 2.5 cm, and a maximum radius  $r_{max}$  of 50 cm. Optimal normal vectors were selected adaptively for cylindrical domain fitting, with a fitted

cylinder radius  $\ r_{cyl}$  of 30 cm, and a maximum cylindrical depth  $d_{max}$  of 1.0 m.

Figure 5 presents the results of change detection on slope structures using C2C (Ggirardeau-montaut et al. 2005), C2M (Monserrat et al. 2008), and our method. In the figure, unchanged areas are marked in blue, while red areas indicate locations where significant changes have occurred. Green areas represent misidentified regions—those that exceed a preset threshold but do not actually reflect meaningful changes in the model.

The determination of misidentified areas was validated by examining high-resolution UAV images. This validation revealed that the differences between the two-phase models in the green areas were due to minor coordinate deviations remaining after registration, rather than substantial changes such as slope soil loosening or crack expansion. Consequently, these areas were classified as regions of non-real change.

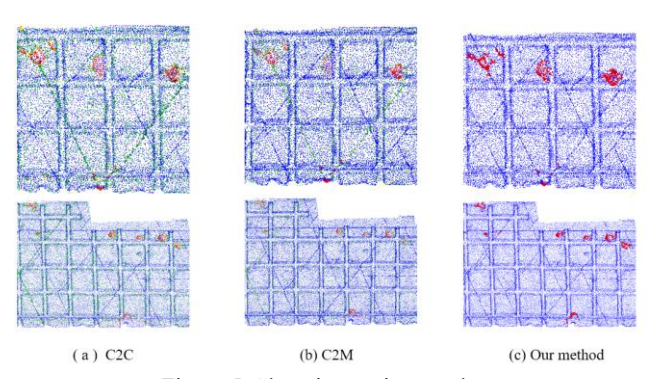


Figure 5. Slope inspection results.

Based on the calculated change distances, the identified change areas can be initially categorized into yellow and red regions. As illustrated in Figure 6, the results of slope structure change detection show that yellow areas represent slight changes, which may be characterized by minor vegetation cover or slight soil erosion. In contrast, red areas indicate significant changes, potentially involving more severe soil structure loosening or localized subsidence.



Figure 6. Results of the classification of areas of slope change.

#### 3.3 Experimental analysis

After completing the slope change detection, this study assesses the recognition accuracy and misrecognition rate of our algorithm across various thresholds. Recognition accuracy is defined as the ratio of the number of change regions identified by the algorithm to the total number of actual change regions present. In contrast, the false recognition rate is defined as the ratio of incorrectly identified regions to the total number of recognized change regions.

The results indicate that the choice of thresholds significantly affects detection accuracy. Lower thresholds enhance the rate of change detection but also increase the likelihood of false identifications, as they are more susceptible to noise and registration residuals. Conversely, higher thresholds reduce the rate of false alarms but may lead to the omission of moderate deformations, thereby compromising the completeness of the detection.

Table 1 presents the recognition accuracies and false recognition rates at various thresholds, offering a quantitative foundation for the subsequent analysis of the results.

Threshold (mm)	Ccorrect area	Wrong area	Actual change	Aaccuracy (%)	False rate (%)
1	61	7	63	96.825	10.294
3	60	4	63	95.238	6.25
5	57	3	63	90.476	5.0
7	55	1	63	87.302	1.786
9	51	0	63	80.952	0.0
10	46	0	63	73.016	0.0

Table 1. Recognition accuracy and false recognition rate under different thresholds

As shown in Table 1, as the threshold increases, both the number of correctly recognized change regions and the number of incorrectly recognized regions exhibit a decreasing trend, leading to an overall decline in recognition accuracy. At a threshold value of 1 mm, the number of correctly recognized regions reaches its maximum, with a recognition accuracy of 96.825%; however, the false recognition rate is relatively high at 10.294%. When the threshold is raised to a certain critical value, the false recognition rate drops to 0%, but detection accuracy falls to a minimum of 73.016%, resulting in a significant risk of missed detections. This indicates that a lower threshold facilitates the identification of more change regions but increases the likelihood of misidentification, while a higher threshold reduces misidentification at the cost of potentially overlooking some actual change regions.

Based on this analysis, this paper determines the optimal threshold value according to practical requirements. The change regions identified by the algorithm are labeled in the model, as illustrated in Fig. 7. Through this model labeling, the distribution of change areas in slopes and drains can be clearly observed, with several representative change areas highlighted in red.



Figure 7. Model labeling results.

As illustrated in Figure 7, changes in the slope structure are primarily concentrated in areas of surface damage attributed to vegetation growth. This is evidenced by local cracks in the surface soil, which occur due to the expansion of the root system. The growth of the vegetation root system not only damages the surface layer of the slope but may also lead to the loosening of the soil structure, thereby increasing the risk of landslides and reducing slope stability. The detection results indicate that the algorithm proposed in this paper provides valuable data support for the protection of railroad slopes and holds practical significance for ensuring line safety.

### 4. Conclusion

We proposed in this study for the automatic detection of changes in railroad slopes is based on a biphasic oblique photographic model. It identifies areas of change through a structured process that includes extracting the vertex point cloud data of the structure, followed by preprocessing steps such as up-sampling to increase density while preserving features, and alignment to eliminate spatial offsets caused by coordinate discrepancies. Subsequently, core points are selected, normal vectors are calculated, and cylindrical analysis domains are constructed to facilitate comparisons between the biphasic point clouds within these domains, focusing on the differences in projected scales.

Experiments conducted on data from the Nanwan Railway section in Xinzhou, Shanxi, demonstrate that this method outperforms traditional techniques, such as C2C and C2M. It accurately extracts significant variations at comparable thresholds while effectively filtering out unrealistic interferences, such as residual alignment bias. An analysis of accuracy and false recognition rates across different thresholds confirms that the appropriate selection of thresholds strikes a balance between these metrics, thereby minimizing the risks of excessive underdetection or false recognition.

Moreover, marking changes in the model allows for the visualization of their locations and extents, thereby guiding maintenance efforts, supporting dynamic health assessments, advancing whole-life intelligent maintenance, reducing costs, and enhancing railroad safety.

# Acknowledgement

This study is sponsored by the BUCEA Categorical Development Quota Project-Postgraduate's Innovation Project.(PG2025141)

## References

Deng, Z. X., Xu, L. R., Li, Y. W., Wang, W, B., Su Q., 2025: Pr ediction of cumulative deformation of high-speed railway subgr ade based on experience-constrained neural network. *Journal of Railway Science and Engineering*, 22(2), 469-484. doi.org/10.1 9713/j.cnki.43-1423/u.T20240651.

Dong, H. R., Wang, T., Song, H. F., Liu, Z., Zhou, D., 2024: A change detection approach based on multi-temporal SAR image s for railway perimeter intelligent perception. *IEEE Transaction s on Industrial Cyber-Physical Systems*, 2, 435-445. doi.org/10. 1109/TICPS.2024.3452644.

- Girardeau-Montaut, D., Roux, M., Marc, R., Thibault, G., 2005: Change detection on points cloud data acquired with a ground l aser scanner. *International Archives of Photogrammetry, Remot e Sensing and Spatial Information Sciences*, 36, 30-35.
- Liu, H., Wang, S., Jing, G., Yu, Z., Yang, J., Zhang, Y., Guo, Y., 2023: Combined CNN and RNN neural networks for GPR detection of railway subgrade diseases. *Sensors*, 23(12), 5383. doi.org/10.3390/s23125383.
- Monserrat, O., Crosetto, M., 2008: Deformation measurement u sing terrestrial laser scanning data and least squares 3D surface matching. *ISPRS Journal of Photogrammetry and Remote Sensing*, 63(1), 142-154. doi.org/10.1016/j.isprsjprs.2007.07.008
- Mukupa, W., Roberts, G. W., Hancock, C. M., Al-Manasir, K., 2017: A review of the use of terrestrial laser scanning application for change detection and deformation monitoring of structures. *Survey Review*, 49(353), 99-116. doi.org/10.1080/00396265.20 15.1133039.
- Ouyang, Y., Yi, S., 2020: Modern railways, modern education a nd economic development: an empirical study on the impact of modern railways on economic development in modern China. *J ournal of Xiangtan University (Philosophy and Social Sciences)*, 44(5), 58-67. doi.org/doi:10.13715/j.cnki.jxupss.2020.05.010.
- Ren, S. Q., He, K. M., Girshick, R., Sun, J., 2017: Faster R-CN N: towards real-time object detection with region proposal netw orks. *IEEE Transactions on Pattern Analysis and Machine Intel ligence*, 39(6), 1137-1149. doi.org/10.1109/TPAMI.2016.25770 31
- Shao, J. H., Zheng, W. P., Zhang, B., Du, Y., Wang, X. T., Lua n, J. H., 2023: Slope defect identification of loess highway base d on point cloud data. *Rock and Soil Engineering Technology*, 3 7(3), 320-326.
- Yu, J. Y., Xue, X. K., Chen, C. F., Chen, R. P., He, K. Y., Li, F., 2022: 3D reconstruction and disaster identification of highway slopes based on UAV oblique photography. *China Journal of H ighway and Transport*, 35(4), 77-86. doi.org/10.19721/j.cnki.10 01-7372.2022.04.005.
- Zhang, W., Wen, Z., Kang, Y., Liu, Y., Guo, L., Su, F., Yu, Q., Wang, X., 2024: Investigation on Moisture-Heat-Deformation B ehaviors of the Ordinary Railway Subgrade in Seasonally Froze n Regions. *International Communications in Heat and Mass Tr ansfer*, 159, 108208. doi.org/10.1016/j.icheatmasstransfer.2024. 108208
- Zhang, Z. C., Vosselman, G., Gerke, M., Persello, C., Tuia, D., Yang, M. Y., 2019: Detecting Building Changes between Airbo rne Laser Scanning and Photogrammetric Data. *Remote Sensing*, 11(20), 2417. doi.org/10.3390/rs11202417.